IN SITU TRANSMISSION ELECTRON MICROSCOPY ION IRRADIATIONS OF MODEL IRON-CHROMIUM ALLOYS

BY

CAROLYN ANNE TOMCHIK

THESIS

Submitted in partial fulfillment of the requirements
for the degree of Master of Science in Nuclear Engineering
in the Graduate College of the
University of Illinois at Urbana-Champaign, 2011

Urbana, Illinois

Master's Committee:
Professor James F. Stubbins, Director of Research
Professor Brent J. Heuser

Abstract

Iron-chromium alloys are used as a model to study the microstructural evolution of defects in irradiated structural steel components of a nuclear reactor. We examine the effects of temperature and chromium concentration on the defect evolution and segregation behavior in the early stages of damage. *In situ* irradiations are conducted in a transmission electron microscope (TEM) at 300°C and 450°C with 150keV iron ions in single crystal Fe14Cr and Fe19Cr bicrystal to doses of 2E15 ions/cm^2. The microstructures resulting from annealing and irradiation of the alloy are characterized by analysis of TEM micrographs and diffraction patterns and compared with those of irradiated pure iron. We found the irradiation temperature to have little effect on the microstructural development. We also found that the presence of chromium in the sample leads to defect populations with small average loop size and no extended or nested loop structures, in contrast to the populations of large extended loops seen in irradiated pure iron. A very weak dependence was found on the specific chromium content of the alloy. Chromium was shown to suppress defect growth by inhibiting defect mobility in the alloy. While defects in pure iron are highly mobile and able to grow, those in the FeCr alloys remained small and relatively motionless due to the pinning effect of the chromium.

Acknowledgements

I would like to thank my advisor, Prof. James F. Stubbins, for his support and advice throughout my undergraduate and graduate studies. I appreciate the freedom he has given me to pursue my own interests and the countless opportunities he has given me to travel and share my research with new people. He has become a mentor and a friend to me, and for that I am grateful.

I would also like to thank Mark Kirk of Argonne National Laboratory for his friendship, guidance, feedback, and help while I completed this work. His expertise in operating the TEM was invaluable, and his advice about being a successful researcher was much appreciated.

Many thanks are also owed to Pete Baldo at Argonne National Laboratory for running the accelerator so flawlessly that I could finish all of my irradiations in the time I was given. I can't thank Pete enough for making this possible.

I would like to thank my friends and colleagues in Dr. Stubbins' research group, past and present, for their support. In particular, I'd like to thank Maria Okuniewski for being an inspiration and role model for me. I'd also like to thank two colleagues I met in my travels for offering valuable encouragement and feedback on my work, Djamel Kaoumi and Zhongwen Yao.

I would like to thank Prof. Brent J. Heuser for his valuable feedback and suggestions.

Thank you to my family, the Lachners, Litwins, and Tomchiks, for supporting me. To my husband, Ed, and my dog, Persie, I couldn't have finished this without your love and support.

I owe my most heartfelt thanks to my friend Ian, who is infinitely patient, supportive, and helpful to me. His inquisitive nature and dedication to good research practice has inspired me to keep working through the ups and downs of my work.

Table of Contents

Chapter 1

INTRODUCTION

1.1 MOTIVATION AND PREVIOUS WORK

In order for research and development efforts on Generation IV and fusion reactor systems to advance, a better understanding is required of the processes taking place in the structural components of the reactor under irradiation at high temperature. Predictive multiscale models for radiation damage must be developed so that we can optimize structural materials and analyze the long-term effects of irradiation and temperature on material strength. In order to develop and validate multiscale models, we need experimental benchmarks. In this work, we establish simple benchmarks by conducting experiments on model reactor structural materials. The use of model materials provides a simplified case on which to test theoretical models.

Ferritic alloys form the basis of proposed structural materials for Generation IV and fusion reactors. Ferritic alloys (iron-base alloys with body-centered cubic structure) show superior irradiation resistance when compared with austenitic alloys (iron-base alloys with face-centered cubic structure). Ferritic-martensitic steels are considered good candidates for structural applications in nuclear systems because of their low activation and resistance to radiation-induced swelling. Chromium content provides corrosion resistance but may also lead to embrittlement, particularly at lower temperature. Iron-chromium based alloys also exhibit a low ductile-to-brittle transition temperature with a minimum shift in ductile to brittle transition temperature (ΔDBTT) at approximately 9% chromium, as shown in Figure 1.1. It is not known what causes the increase in ΔDBTT at concentrations above 9% chromium, but it is thought to

relate to the development of chromium-rich precipitates. Chromium content also affects both the fracture behavior and the void swelling response of the alloy [1-5]. While Fe is the simplest model material, the effect of chromium content on the evolution of irradiation defected microstructures needs to be examined further. Therefore, binary FeCr is used as our simple model to represent this class of materials.

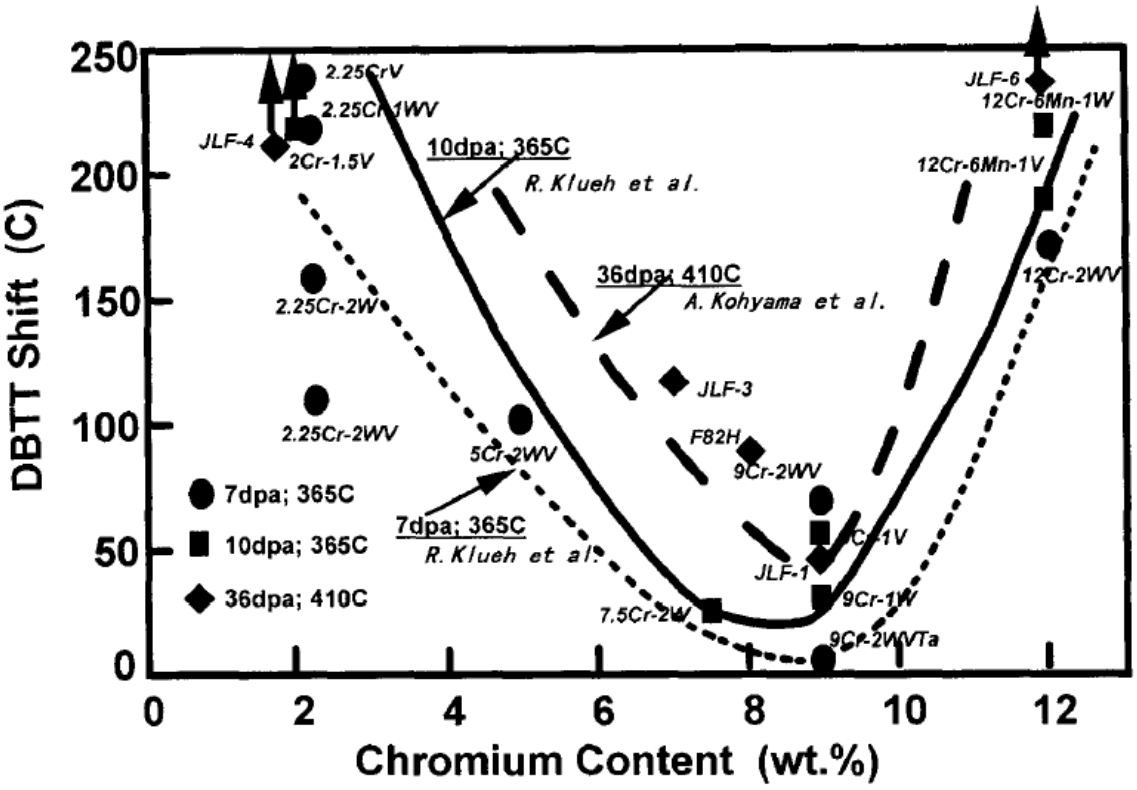

Figure 1.1. Dependence of DDBTT on Chromium content of the alloy, taken from [3].

Because of the cost and limited availability of neutron irradiation facilities, we use ions to simulate neutron radiation damage. In order to provide the opportunity for *in situ* observation of the damage accumulation, these irradiations can be done *in situ* in a TEM using thin foil samples. The justification for using ion irradiations of thin films as a model for bulk neutron irradiation is

presented in section 1.3. Examinations have been made in this manner on Fe and some FeCr thin films. Okuniewski [6] conducted 300C and 450C positron and Fe+ irradiations on ultra-high purity (UHP) iron, finding the development of extended and nested defect loop structures at doses greater than $4x10^{18}$ ions/m^2 (1.42 dpa). Yao, *et al.* conducted room temperature and 300C Fe+ and Xe+ irradiations of polycrystalline UHP Fe, Fe5Cr, Fe8Cr, Fe11Cr, and single crystal Fe9Cr and Fe18Cr [7]. They found that the addition of chromium to the samples seemed to cause pinning of defects, preventing them from forming the dynamic and extended structures seen in the pure Fe samples. They found there to be little difference between the different chromium contents. This study expands on these works by performing high temperature (300C and 450C) ion irradiation experiments on thin films of Fe11Cr and Fe18Cr, examining both the effects of irradiation temperature and chromium content on the microstructural evolution of the samples.

1.2 FACILITY OVERVIEW

Irradiations were conducted *in situ* at Argonne National Laboratory's Intermediate Voltage Electron Microscope (IVEM-Tandem) facility. The IVEM is a Hitachi H-9000 that is interfaced with an ion accelerator to enable an ion and electron beam to be simultaneously incident on a sample. This allows for *in situ* observations of defect formation and evolution. The microscope is also equipped with a Gatan double-tilt heating stage to allow sample irradiations to be done at high temperature. Figure 1.2 shows the IVEM-Tandem facility. The ion beam line can be seen coming in from the top left of the photo; it is angled 30 degrees away from the microscope column axis. Figure 1.3 shows the relative orientation of the beam lines to the sample and the screen. The beam of ions incident on the sample has a diameter of approximately 1.5mm. The

IVEM voltage is variable from 100 to 300kV, but was operated at 200kV for these experiments. The vacuum at the sample can usually be maintained at around 10^{-7} Torr. TEM images can be recorded by film, CCD camera, and a Gatan image-intensified camera for DVD recording.

Figure 1.2. The IVEM-Tandem at Argonne National Laboratory [8].

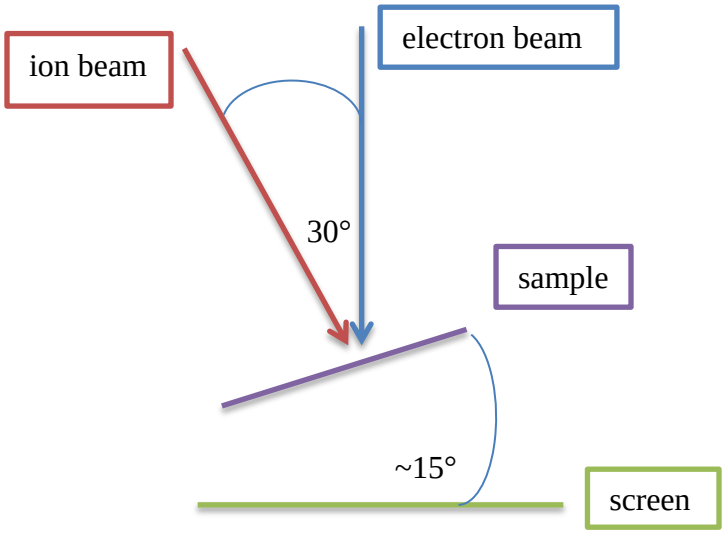

Figure 1.3. The orientation of the sample with respect to the electron and ion beams.

1.3 BACKGROUND SCIENCE

1.3.1 *In situ* Ion Irradiations of Thin Films

As we are conducting basic, systematic research in order to provide benchmark conditions for modeling efforts, we need to be able to collect data at a wide range of dose points at specific temperatures. We are not able to easily accomplish this using neutron irradiations for a variety of reasons. Firstly, access to neutron irradiation facilities is very limited. Secondly, irradiations in a test reactor usually take years to set up, perform, and analyze. Precisely controlling each of several parameters (dose, dose rate, temperature) in a test reactor can be difficult if not impossible. The irradiated samples then require an activity analysis and specialized handling in a hot cell. The cost and degree of difficulty of neutron irradiations, therefore, is very high.

Ion irradiations provide considerable advantages over neutron irradiations in terms of simplicity of setup, access to facilities, ease of controlling parameters, and cost. In general, heavy ion irradiations can be performed up to doses of five or so dpa in a matter of hours to days,

depending on the type and energy of the irradiating ion. The dose and dose rate can be much more easily controlled, and the irradiation produces little to no activity in the samples. This allows samples to be transported and analyzed at a variety of different facilities that wouldn't be equipped to handle hot samples. The challenge is to justify the use of ions as a surrogate for neutrons in irradiation studies. We need to understand how the use of ions instead of neutrons may change (or not) the nature and morphology of the defected microstructure. Keep in mind that for our purposes, directly replicating the conditions of a neutron irradiation is not required. Instead, we aim to provide conditions under which the same microstructural development will occur so that we can examine the defect kinetics *in situ*.

The first key to being able to use ions as a surrogate for neutrons in irradiation studies is to have a common representation of dose - a way to convert from particle fluences to damage in the samples. We use the unit of displacements per atom (dpa). The first model for determining the damage produced in the sample (in terms of dpa) was developed by Kinchin and Pease [9] and was modified into the now commonly used NRT model [10]. The NRT model gives that the number of Frenkel pairs ν(T) generated by a primary knock-on atom (PKA) of energy T is given by:

$$\upsilon(T) = \frac{\kappa E_D(T)}{2E_d}$$

Where κ is is the displacement efficiency (for the NRT modified Kinchin and Pease model, 0.8 is used), $E_D(T)$ is the damage energy (the energy of the PKA minus the energy loss to electron excitation), and E_d is the displacement energy (the energy required to displace the hit atom from its lattice position). To determine the NRT dpa we integrate the damage function over the recoil spectrum and time to obtain [12]:

$$dpa = \phi\sigma_{FP}t = \phi t \frac{dT\big(d\sigma(E < T)\big)}{dT} \upsilon(T)$$

Now that we have a common measure of damage to the sample, dpa, we must examine how the damage morphology differs between ion and neutron irradiated samples. Figure 1.4 shows the different damage morphologies created by several irradiating particles. As is shown in the figure, heavy ions can produce dense cascades similar to those seen in neutron irradiations. The damage profile for heavy ions is also sharply peaked, but we have chosen the irradiating ion energy (150keV Fe+) such that the peak will occur within the thin foil (at 28nm depth), as verified by SRIM calculations [13].

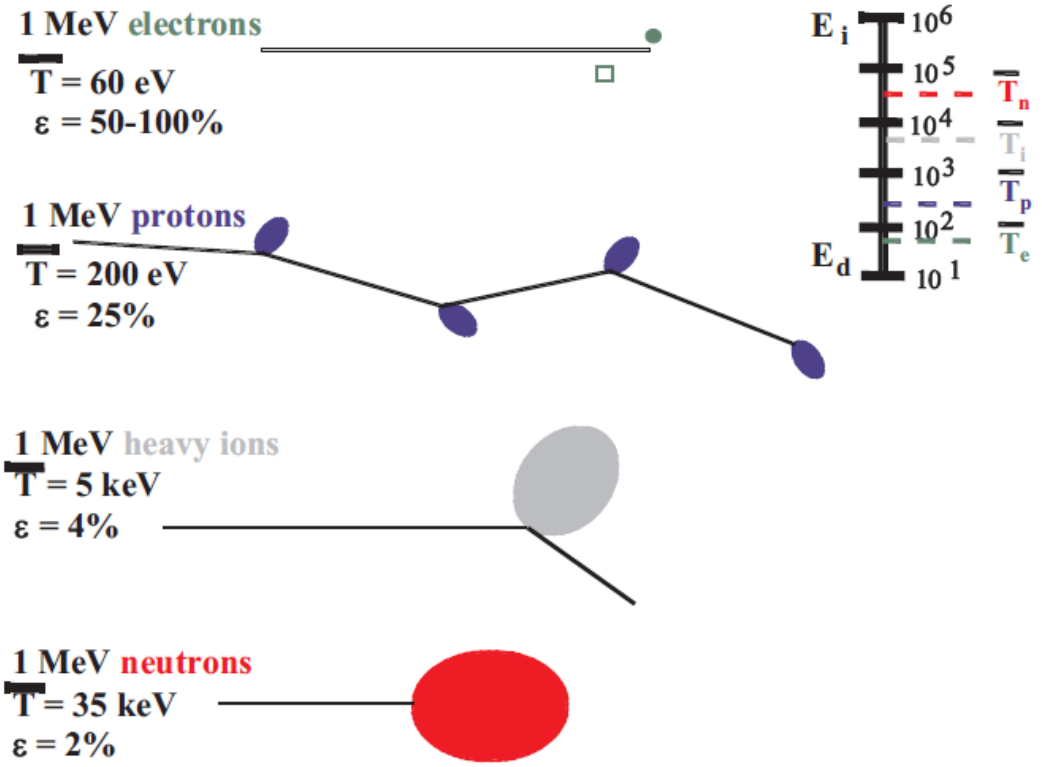

Figure 1.4. Different damage morphologies, displacement efficiencies (ε), and average recoil Energies (T) for 1 MeV particles of different type incident on nickel [12].

The dose rate for these ion irradiated samples will not be comparable to neutron irradiated samples (it will be much higher, so substantial doses are acquired quickly, which is one of the advantages of doing these irradiations with heavy ions). We can use relations developed by Mansur [14-16] in order to account for the difference in dose rates between these and neutron irradiation experiments. These invariant calculations were developed in order to better understand the effect of changes in irradiation variables (such as dose, dose rate, and temperature) on void swelling. When one of the variables is changed, a shift in the other variables can be performed in order to conserve a physical quantity that describes the behavior of defects during irradiation. For example, in the steady-state recombination dominant regime, for the number of defects absorbed in the sinks (N_s) to be considered as invariant at a constant dose for a given change in dose rate (K), the temperature (T) shift required is given by [16]:

$$T_2 - T_1 = \frac{\left(\frac{kT_1^2}{E_v^m}\right)\ln\left(\frac{K_2}{K_1}\right)}{1 - \left(\frac{kT_1}{E_v^m}\right)\ln\left(\frac{K_2}{K_1}\right)}$$

Where E_v^m is the vacancy migration energy.

As a consequence of conducting irradiations in a thin foil, we must account for two very large sinks (each of the free surfaces) in close proximity to the dislocation loops that will form under irradiation. We know that we will lose some orientations of glissile loops to the surfaces during irradiation, and that this loss will be highly dependent upon the foil orientation. Care must be taken, therefore, to note the orientation of the foil and to note that loops formed in the glide planes of the crystal will likely be lost to the surface.

1.3.2 TEM Characterization of Defects in Thin Films

Transmission electron microscopy (TEM) is a widely used method of material characterization, and several texts exist explaining its theory and practical technique [17-19]. However, little has been written on the use of TEM to characterize radiation damage in particular, the exception being the text by Jenkins and Kirk [20]. Depending on the type of defect under investigation, there are several different imaging techniques at our disposal. Radiation-induced defects can be particularly tricky to image since they are initially very small and oftentimes do not resolve their image fully into contrasting loops, instead developing only into small loops with dot-type contrast. Here we will discuss briefly some of the techniques available for imaging defects, focusing in particular on the weak beam dark field (WBDF) technique, which has been shown to be especially useful for imaging small defect clusters.

Contrast in a TEM images arises due to scattering of the incident electron beam by the sample material. As it travels through the material, the electron wave can change both its amplitude and its phase. Each of these changes leads to contrast in the image – amplitude contrast or phase contrast. Here we will address only amplitude contrast. There are two fundamental ways to form images using amplitude-contrast, namely, bright field (BF) and dark field imaging (DF). Figure 1.5 shows the necessary positioning of the objective aperture with respect to the diffraction pattern to form either a bright or dark field image. The aperture selects which electrons will make up the image. A bright field image is formed by selecting the electrons in the direct beam to form the image. A dark field image will be formed by placing the aperture around a diffracted beam, so an image will be formed only by electrons scattered in that particular direction.

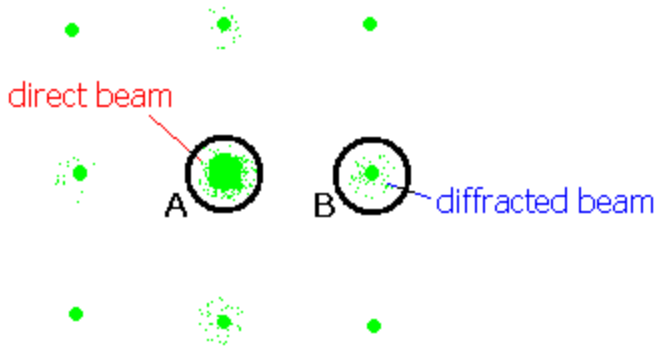

Figure 1.5. The relative positioning of the objective aperture in order to form A) a bright field image or B) a dark field image. The objective aperture is represented by the black circle.

There are two main types of amplitude contrast: mass-thickness contrast and diffraction contrast. Mass-thickness contrast arises when electrons are incoherently scattered (Rutherford scattering). Areas of the sample that are thicker or have higher atomic mass number (Z) will scatter more electrons off axis than those that are thinner or lower-Z. Therefore fewer electrons from the thicker or higher-Z region will fall on the corresponding area of the image plane, making it appear darker on the screen in a BF image. Diffraction contrast arises from coherent elastic scattering of electrons into specific (Bragg) angles. Defects become visible due to their elastic strain fields. The strain field around the defect causes changes in the diffracting conditions in the local area, leading to local contrast.

Figure 1.6 shows three of the different diffraction conditions used in diffraction-contrast imaging: two-beam dynamical conditions, kinematical bright field conditions, and weak beam dark field conditions. Two-beam dynamical conditions are achieved when the sample is tilted so that one set of the diffracting planes (hkl) is at or very near to the Bragg condition. We can refer to this condition in terms of the deviation parameter (or excitation error), s_g, the distance of the

reciprocal lattice point $\boldsymbol{g}$ from the Ewald sphere. In this case, then, we can say that $s_g \approx 0$. This means that the diffracted beam $\boldsymbol{g}$ will appear at a similar intensity to the direct beam, hence the "two-beam" dynamical condition. The contrast achieved is particularly sensitive to weak lattice strains, so it is well-suited to the study of small dislocation loops. However, due to the strong dynamical interaction between the two beams, the image characteristics of the defects will be complex, exhibiting black-white lobe contrast. This contrast can be exploited in order to deduce the Burgers vectors and habit planes of the loops, provided one can tilt to several different diffracting conditions. The contrast does not, however, correspond to the physical size of the defects. Bright-field kinematical conditions can be used to avoid the dynamical contrast effects seen under two-beam dynamical conditions. The bright-field kinematical condition requires setting a two-beam condition with a small deviation parameter ($s_g > 0$). Here the images become narrower, condensing into small black dots or loops, and the contrast is more representative of the physical size of the defect cluster.

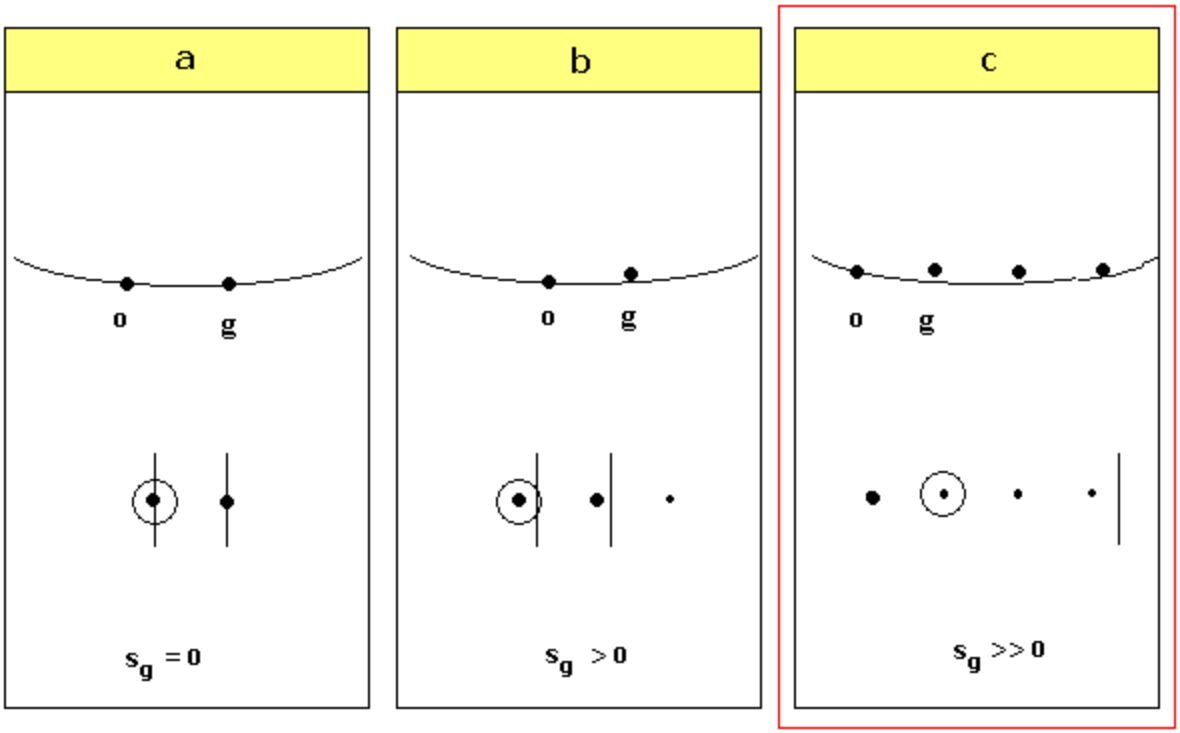

Figure 1.6. Positions of the diffracted beams with respect to the Ewald sphere as well as the objective aperture and Kikuchi lines for a) two-beam dynamical conditions, b) kinematical bright field conditions, and c) weak-beam dark field conditions.

Weak beam dark field imaging involves obtaining useful information from a weakly excited beam. The sample is tilted such that in regions far away from defects the diffracting planes are far away from the Bragg condition (therefore, $s_g >> 0$). Contrast in weak beam dark field images comes from regions of large lattice strain near the defect cores. Because the sample is tilted far from the Bragg condition, the intensity of the image is very low. High relative intensity, however, appears in regions close to defects where the local strain field can bend the reflecting planes back towards the Bragg condition. Weak beam dark field images are therefore of low intensity but high relative contrast.

In order to obtain useful information from WBDF images, the deviation parameter must be set such that:

$$|s_g| \geq 2 \times 10^{-1}\text{nm}^{-1}$$

This condition allows for a narrow peak of high-contrast to appear near the defect core. In these experiments, this condition allowed for visibility of the most defects. In order to set this necessary value for the deviation parameter, we refer to the Kikuchi lines in the diffraction pattern. The sample is tilted as shown in figure 1.6 c), such that the Kikuchi line cuts through the line of systematic reflections at $n\boldsymbol{g}$ (note n does NOT have to be an integer, and indeed it shouldn't be for the best image resolution). The objective aperture is placed over the first diffracted beam. This condition is written as ($\boldsymbol{g}$, $n\boldsymbol{g}$). In the example shown in Figure 1.6 c), $n \approx 3.5$. The required value of n for a given s_g can be found using simple geometry and referencing Figure 1.7 which shows the Ewald sphere together with the line of systematic reflections and its dimensions.

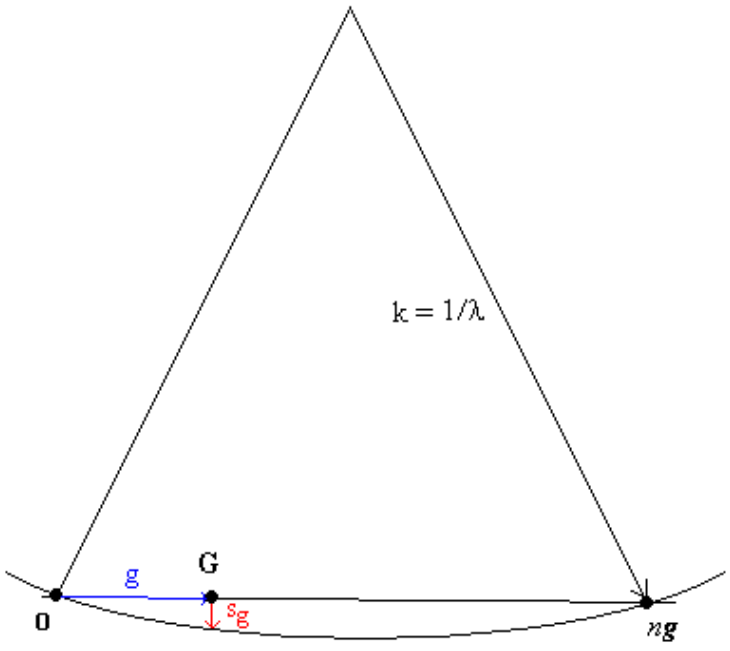

Figure 1.7. The Ewald sphere construction for weak beam dark field imaging showing the relationship between s_g, n, and λ (the wavelength of the electrons).

Using the intersection chord theorem and the fact that $k >> s_g$, we find that:

$$s_g = \frac{(n-1)g^2}{2k}$$

Where $g = 1/d_{hkl}$ is the magnitude of the reciprocal lattice vector $\boldsymbol{g}$ that corresponds to the planes (hkl) with interplanar spacing d_{hkl}. Note for an electron microscope operated at 200kV, $\lambda = .025$ Ang. The narrow intensity peaks observed in weak-beam microscopy are due to the small value of the effective extinction length, ξ_g^{eff} ($1/s_g \approx \xi_g^{eff}$). For $s_g = 0.2$ nm, $\xi_g^{eff} \approx 5$nm, which gives dislocation peak widths of approximately $1/3^* \xi_g^{eff} \approx 2$ nm. In this work and others, defects are clearly most visible in WBDF conditions [21,22]. However, as with any imaging condition, care must be taken not to assume that the image size is directly the size of the defect. Simulation work by Zhou *et al.* shows good agreement between modeled defect sizes and TEM WBDF image sizes, so there is reason to be cautiously optimistic about the correlation [23]. Zhou's work shows that while very small (<2 nm) defects are highly sensitive to the exact imaging conditions, defects larger than ~2 nm show a discrepancy in image and actual defect sizes of ±20%. This implies that measured image size distributions will be broadened relative to actual defect size distributions. While this doesn't provide much assurance for measurements of individual defect sizes, the image size is equally likely to appear larger or smaller than the defect size, so the average image size of a defect population is a reasonably good approximation of the average defect size.

Chapter 2

EXPERIMENTS

2.1 DESCRIPTION OF MATERIALS

Experiments were conducted on two binary model alloys with varying chromium content, namely, Fe11Cr and Fe18Cr. The Fe18Cr was grown as a single-crystal drawn cylinder of 7-10mm in diameter by MaTecK GmbH in Juelich, Germany. The Fe11Cr sample was grown as a columnar grain cylinder of 6-8mm in diameter by Welsch Metallurgy. The grain size in the 11Cr sample was large enough to appear as a single crystal in TEM observations. Spectrographic analysis to determine the exact makeup of the specimens was conducted by an independent laboratory. The results of this analysis by Luvak laboratory are given in atom percent composition in Table 2.1. It should be noted that the Fe11Cr sample contained significant amounts (3.59%) of tungsten, the source of which is unknown. Both samples also contained relatively little carbon (<0.02%). In this experiment, the tungsten is unlikely to affect our results. It acts as an α-phase stabilizer for the alloy and can compete with chromium to develop tungsten rather than chromium-carbides, but with these low levels of carbon we did not see the development of carbides in our samples.

	Fe11Cr Columnar grains	Fe18Cr Single crystal
	%	%
Carbon	.017	.008
Sulfur	<.0010	<.0010
Oxygen	.048	.164
Nitrogen	.002	.002
Aluminum	.002	.001
Cobalt	.008	.004
Copper	.057	.051
Chromium	11.3	18.1
Manganese	.002	.002
Molybdenum	.003	.003
Niobium	.019	.005
Nickel	.005	.004
Phosphorus	<.004	<.004
Silicon	.009	.017
Titanium	.002	.002
Vanadium	.002	.002
Tungsten	3.59	.006
Iron	Remainder	Remainder

No other elements detected in excess of .01%.

Methods: Carbon & Sulfur – Combustion infrared detection – ASTM E 1019-08
Oxygen & Nitrogen – Inert gas fusion – ASTM E 1019-8
All others – Direct current plasma emission spectroscopy – ASTM E 1097-07

Table 2.1. Elemental compositions of Fe11Cr and Fe18Cr, provided by Luvak.

2.2 SAMPLE PREPARATION

Samples were prepared from cylindrical ingots by first cutting 200μm cross-sectional slices using wire electrical discharge machining (EDM). The slices had a (001) normal direction. Cutting slices this thin proved challenging in that oftentimes the slices would come out curled into c-shapes instead of flat. This made further sample preparation difficult. This problem was mitigated by using a thinner wire and a slower cutting speed. The finer wire also minimized the amount of material lost during cutting. A manual punch was used to cut 3mm discs from the

EDM slices (usually 2-3 discs from each slice). The 3mm discs were manually thinned and polished using SiC papers to a grit of 800 and a thickness less than 100μm. Note that polishing to a finer grit at this stage did not improve our final specimen. Thinned samples were stored in anhydrous methanol to prevent oxidation during travel to the IVEM facility.

The thinned 3mm discs were then electropolished on site at Argonne National Laboratory's IVEM facility. It should be noted that electropolishing is the quality-limiting procedure in our sample preparation, so optimizing the polishing conditions at this stage is crucial. Samples were polished using a Struers Tenupol-5 twin-jet electropolisher. High-quality TEM samples are needed for these experiments and so must not exhibit any significant bending or any pitting or etching of their surface. This is accomplished by selecting the appropriate electrolyte and polishing voltage. Experiments revealed the best electrolyte to be 5% perchloric acid solution (70% commercial $HClO_4$ in water) and 95% anhydrous methanol kept at a temperature of -45 to -50°C, cooled with liquid nitrogen. The polishing voltage was optimized at 30V. The flow rate of the jets was set at 70% of the maximum flow rate. The light sensitivity stop value was set to 800 units. Polishing current and time were allowed to vary on each sample but were typically valued at 70-100 mA and 90-150 s, respectively.

Immediately after polishing, the samples were introduced into a series of three rinsing baths. The first rinse was in anhydrous methanol cooled by liquid nitrogen to ~ -60°C, the second rinse in cold anhydrous ethanol, and the third rinse in cold anhydrous methanol. Care must be taken in this step not to introduce any bending in the thin region surrounding the hole in the sample. In order to minimize flow of the rinsing solution through the hole during the rinse, samples were

first placed on pieces of filter paper and then very gently swished in a direction parallel to the surface. The baths help to remove any residual layer of polishing solution that could cause TEM beam contamination. Cooling the baths helps to slow any pitting or etching effect of the remaining acid on the samples [24]. Immediately after polishing, samples were loaded into a double-tilt heating specimen holder and introduced into the TEM to minimize oxidation.

2.3 SAMPLE IRRADIATION

Once the sample was loaded into the microscope, a suitable thin region with no local bending was found and the temperature gradually increased to one of two irradiation temperatures: 300 or 450°C. *In situ* 150keV Fe^+ irradiations began after the sample temperature equilibrated (usually around 10 minutes). The energy of the Fe^+ beam (150keV) was selected so the damage peak would occur within the foil as well as to compare with experiments by Okuniewski and Yao [6,7]. Irradiations were conducted until a steady state microstructure was reached, to maximum fluences of approximately 1E15 ions/cm^2 (~14dpa) at a rate of ~0.002 dpa/second. The microscope was operated at 200kV, which is well below the threshold for Frenkel pair production in Fe (330kV) as well as the displacement energy threshold. Annealing experiments including exposure to the electron beam at each of the two irradiation temperatures were performed as controls. The *in situ* microstructural evolution was recorded to DVD. In addition to observing microstructure development *in situ*, the irradiations were stopped periodically to image the sample in kinematical bright field and weak beam dark field conditions (g, ~3-4g) with $\boldsymbol{g} = 1\bar{1}0$ and take snapshots with a CCD camera. Additionally, the focus was adjusted to ±3000nm defocus in order to look for voids and bubbles at various dose points.

Chapter 3

EXPERIMENTAL RESULTS

3.1 MICROGRAPHS

During each of the 300 and 450°C irradiations, stops were made periodically to capture micrographs at specific fluence points. Snapshots were taken using Digital Micrograph software, generally at 30,000× magnification. As discussed previously, the defects are most visible in weak beam dark field conditions, but background contrast is also coarser which can make defects indistinct from the background. To help decrease ambiguity surrounding defect identification, images were also recorded in kinematical bright field. In all micrographs, the very thin region near the hole in the sample showed extremely low defect density. There was evidence of some thickness threshold beyond which defect density was constant. Figure 3.1 shows this effect. All measurements of defect densities and sizes were made in this constant-density region.

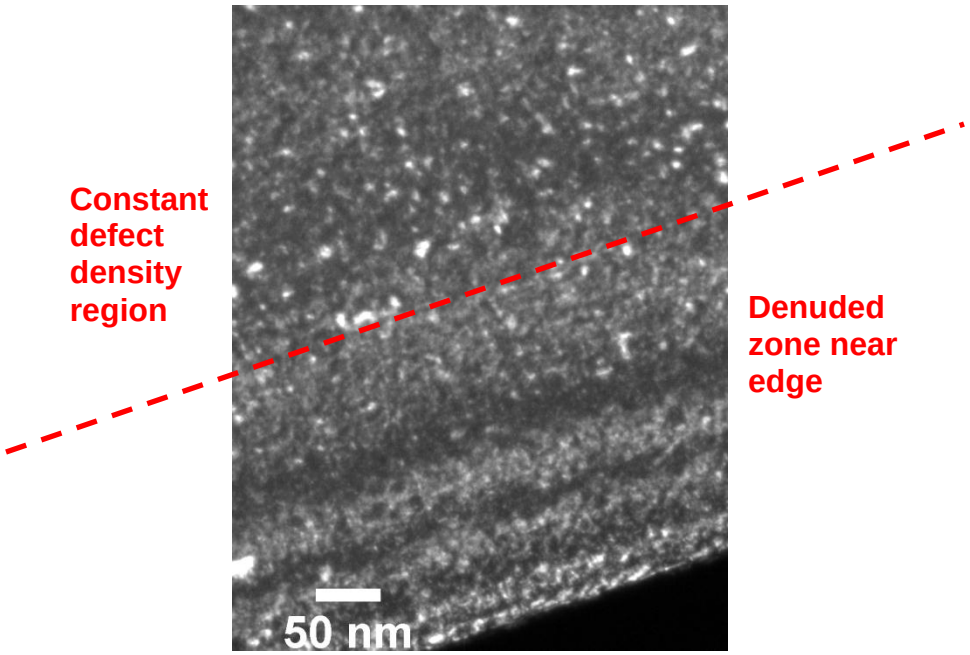

Figure 3.1. Weak beam dark field micrograph of Fe18Cr at 450°C irradiated to 7E14 ions/cm^2 showing thickness threshold for defect stability.

Figure 3.2 shows weak beam dark field (g, ~3-4g) micrographs taken during 450°C irradiations for each of three chromium concentrations – 0%Cr (pure Fe) [6], 11%Cr, and 18%Cr. While the defected microstructures of the Fe11Cr and Fe18Cr appear to evolve similarly, they differ sharply from those seen in pure Fe. Defects first appear as white contrast dots (in dark field) or black contrast dots (in bright field) in all samples, but grow more quickly into extended loop-type structures in pure Fe, appearing as extended loops by a fluence point of 4E14 ions/cm^2. In the Fe11Cr and Fe18Cr samples, by contrast, this fluence point shows defects only as large dots in Fe18Cr and as mostly large dots and a few loop structures in Fe11Cr. With increasing fluence, the structures in pure Fe continue to grow and form extended and even nested loop structures. The FeCr samples, however, show only minimal loop growth with an increasing loop density. As seen in Figure 3.2, some slightly extended structures form at the highest doses in FeCr, but these are difficult to interpret due to very strong background contrast in the micrograph. At several fluence points we also looked through focus for evidence of voids or bubbles; none were found in the FeCr samples. Similar experiments on pure Fe, however, showed evidence of voids at high fluence [6].

Figure 3.3 shows WBDF micrographs of Fe18Cr irradiated at 300 and 450°C. Very little difference is seen in the microstructural evolution of these samples. High densities of defect loops were achieved at a lower fluence in the 300°C irradiations than in the 450°C irradiations. This can be attributed to a loss of more loops to the surface in the early stages of the 450°C irradiation due to increased mobility. As Okuniewski showed in pure Fe case, FeCr also shows more rapid nucleation of defects at lower temperature. We also see a more complicated surface structure at the end of the 450°C irradiation than we do at 300°C. The quality of the surface of

the film degrades more quickly in the high temperature case, making defects more difficult to characterize. We find that temperature has little effect on what is seen in the microstructural evolution of FeCr with increasing irradiation dose. This contrasts with what was found in the Fe system by Okuniewski, who saw the development of large denuded zones in the high temperature case with loss of large loops to the surface [6]. Here the presence of chromium seems to dominate the effect that temperature might have on the evolution of the defected microstructure.

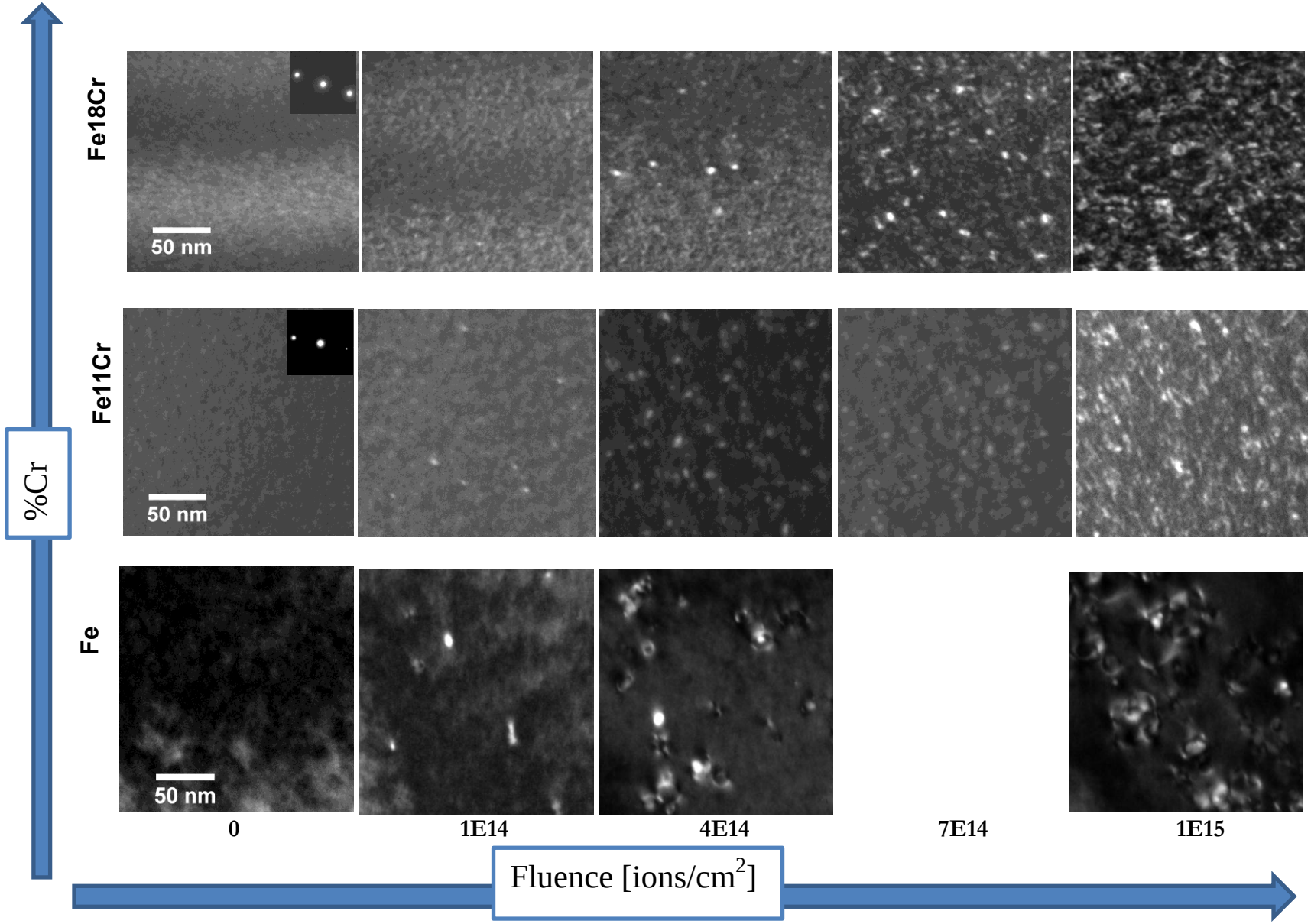

Figure 3.2. WBDF micrographs showing the defected microstructure with fluence as a function of chromium content at 450°C.

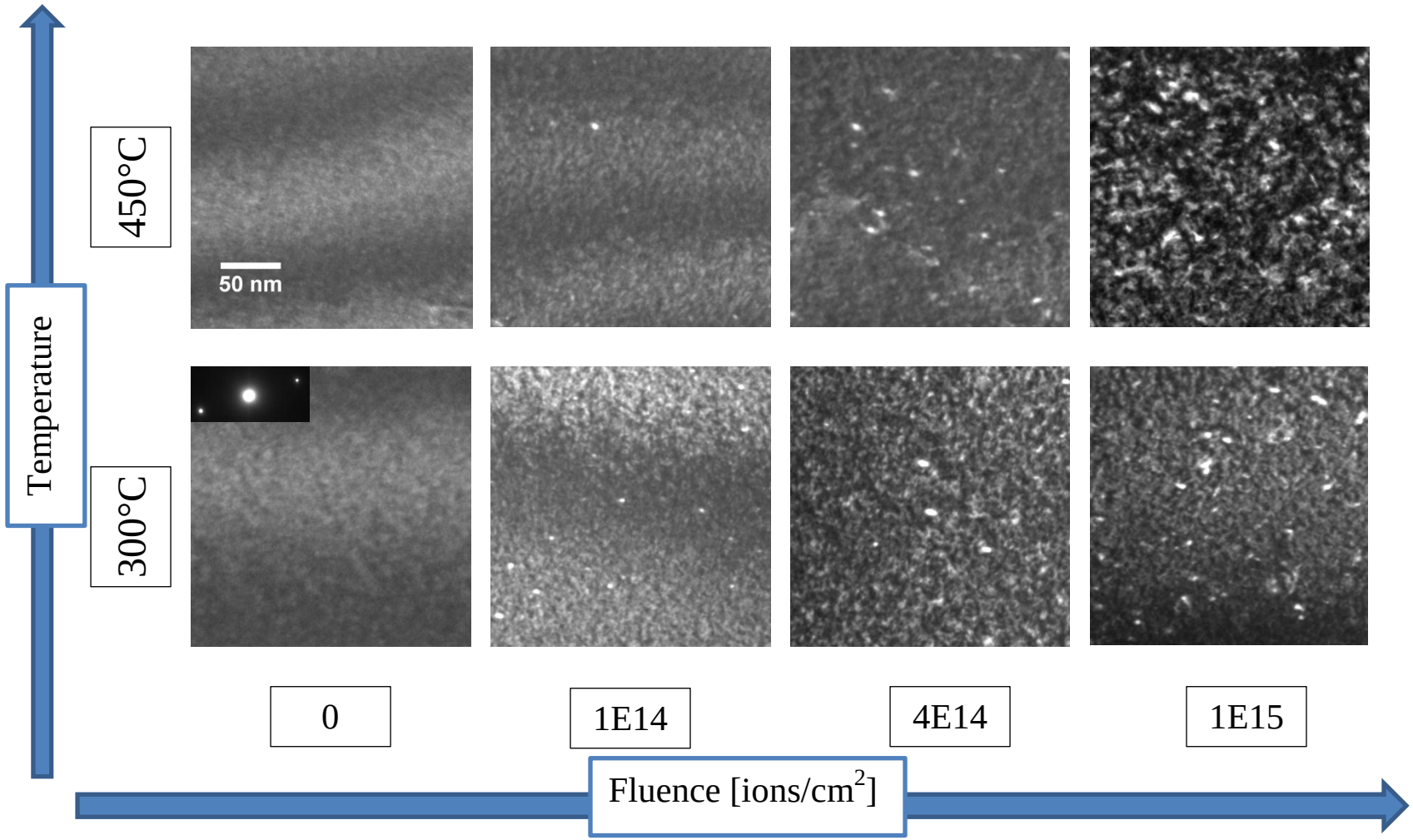

Figure 3.3. WBDF micrographs showing the development of defect microstructure in Fe18Cr with fluence as a function of temperature.

Since we conducted this work *in situ* and recorded DVDs of the irradiations, we have additional insight as to how these microstructures developed. In the pure Fe, defects were seen to move or 'hop' from one location to another, and loops migrated towards one another and combined. In the FeCr alloys, some hopping was occasionally observed, but defects generally appeared and disappeared with very little growth or motion. Note that the disappearance of loops was attributed to glissile loss to the surface of the film. This limited defect mobility within the film in FeCr is what we believe to have prevented the development of the extended structures and voids seen in the pure Fe work. Our work in FeCr reveals a defected microstructure that contains a high density of relatively small defect loops in close proximity to one another. These neighbor defects remain distinct in Fe18Cr; they do not recombine to form larger structures. Figure 3.4 shows a WBDF image of a few defects that have been stable in very close proximity to one another.

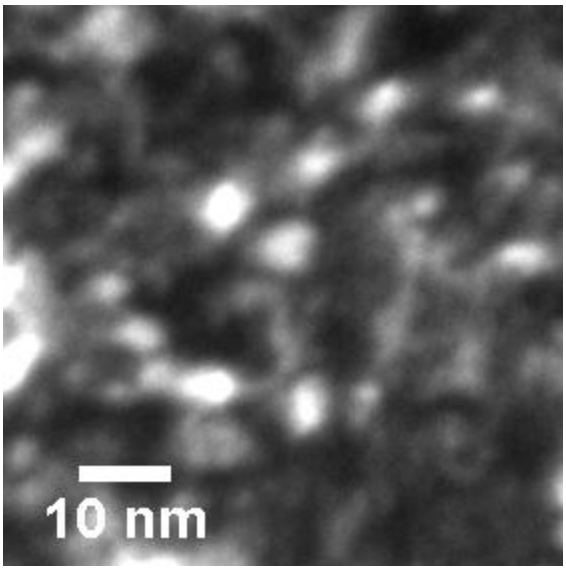

Figure 3.4. Weak beam dark field image of close together but distinct dot-type defects in irradiated Fe18Cr irradiatead at 450°C to a fluence of 1.5E15 ions/cm^2.

It should be noted that some few slightly extended loop-type defects were seen to form in the Fe11Cr irradiations. These defects, while exhibiting loop-type contrast, were much smaller and

less complex than those seen in pure Fe by Okuniewski [6]. A few of these small defect loops are shown in Figure 3.5.

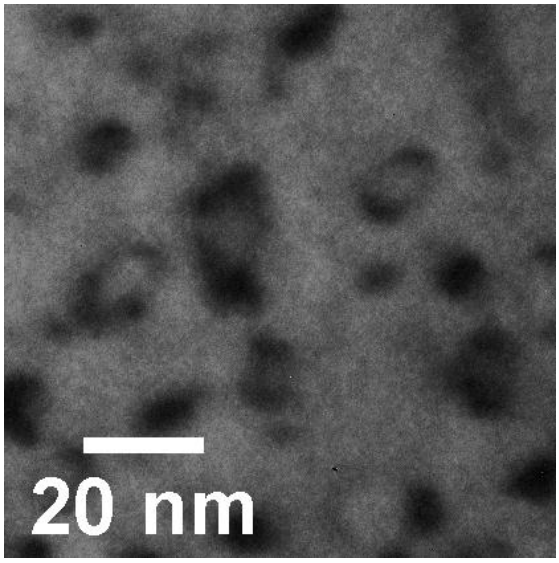

Figure 3.5. Bright field image of defect loops in Fe11Cr irradiated at 450°C to a fluence of 8E14 ions/cm^2.

3.2 DEFECT SIZE DISTRIBUTIONS

The digital micrographs taken at fixed fluence points were analyzed using ImageJ software [25]. Defects were counted and measured across their longest dimension using weak beam dark field micrographs. There is much uncertainty in this analysis, both in terms of distinguishing defects from background contrast and in relating image sizes to defect sizes. No modification was made to the measurements to allow for invisibility of defects when g.b = 0 or to allow for loss of glissile loops to the surface. Figures 3.6 - 3.8 show histograms of defect image size distributions based on measurements made in weak beam dark field.

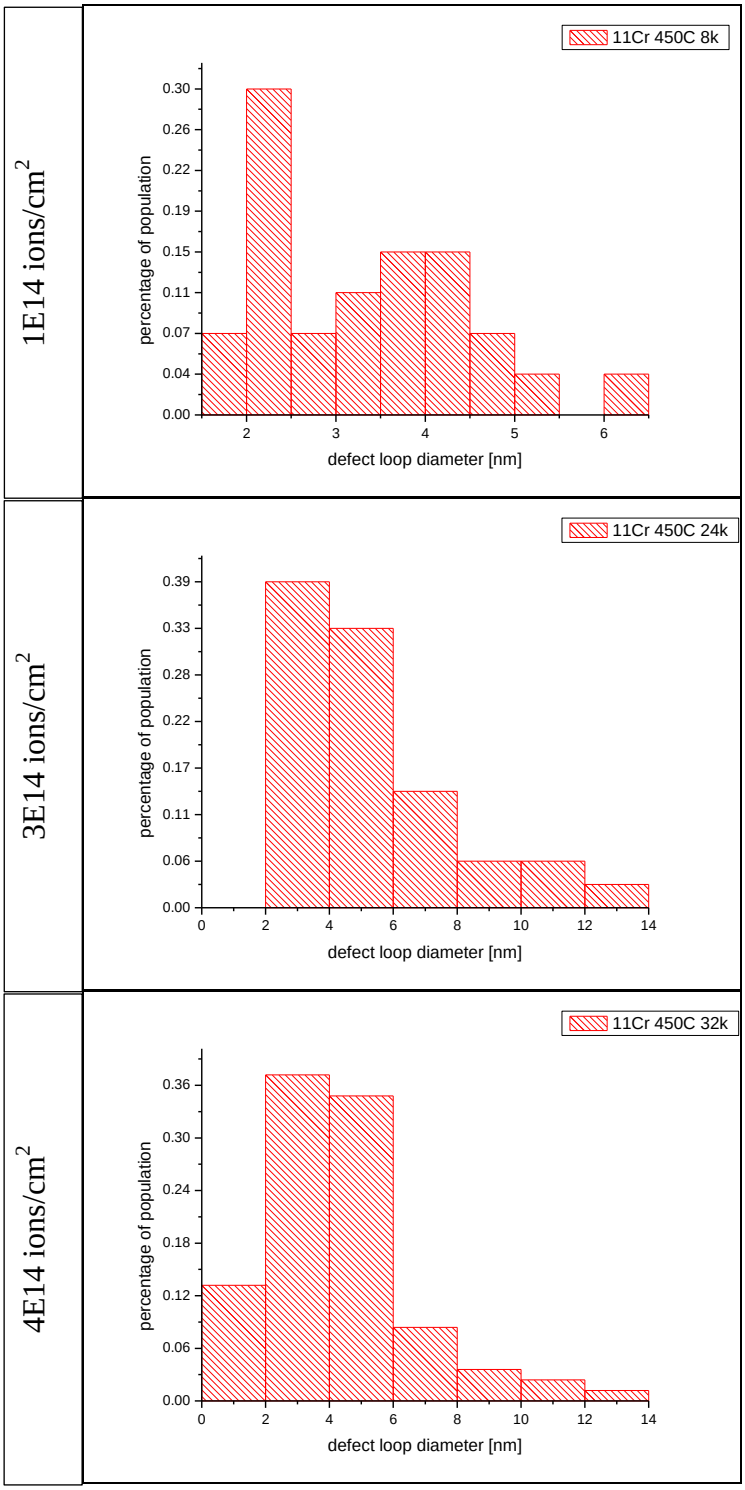

Figure 3.6. Defect population sizes for Fe11Cr irradiated at 450°C at different fluence points, with increasing fluence from top to bottom.

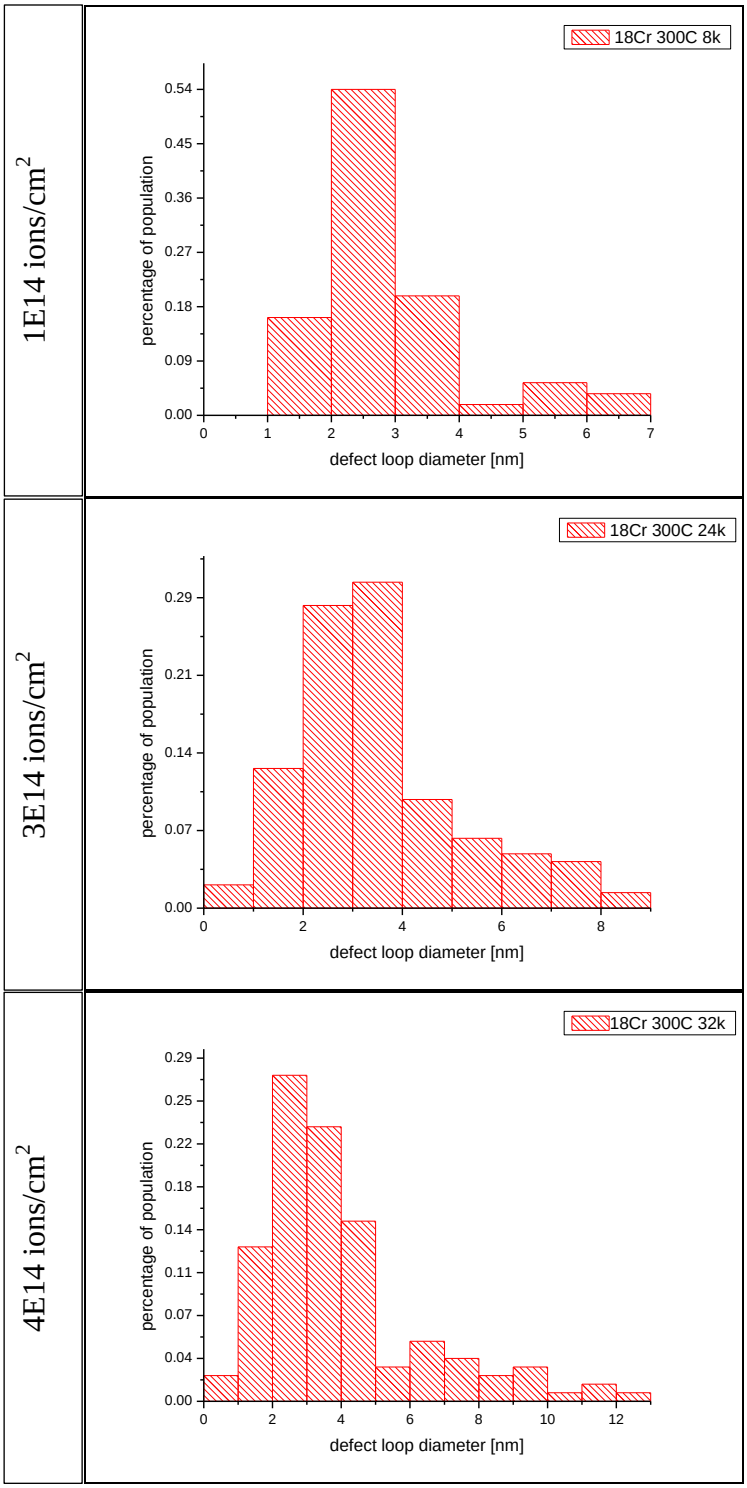

Figure 3.7(a). Defect population sizes for Fe18Cr irradiated at 300°C at fluence points 1E14-4E14 ions/cm^2, increasing fluence from top to bottom.

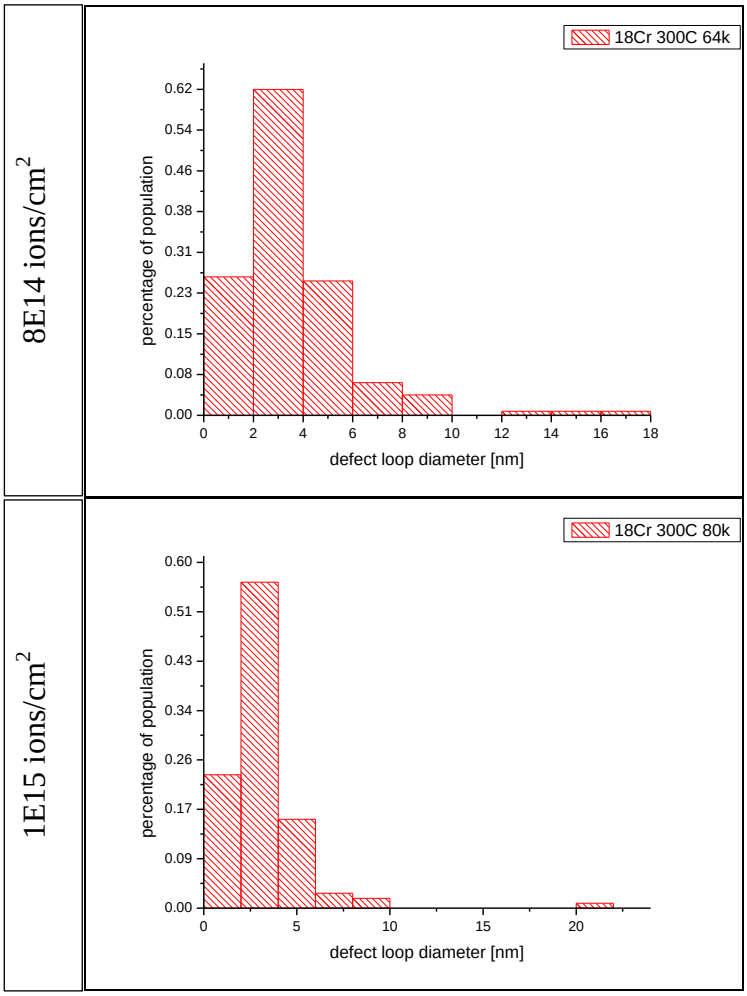

Figure 3.7(b). Defect population sizes for Fe18Cr irradiated at 300°C at fluence points 8E14-1E15 ions/cm^2, increasing fluence from top to bottom.

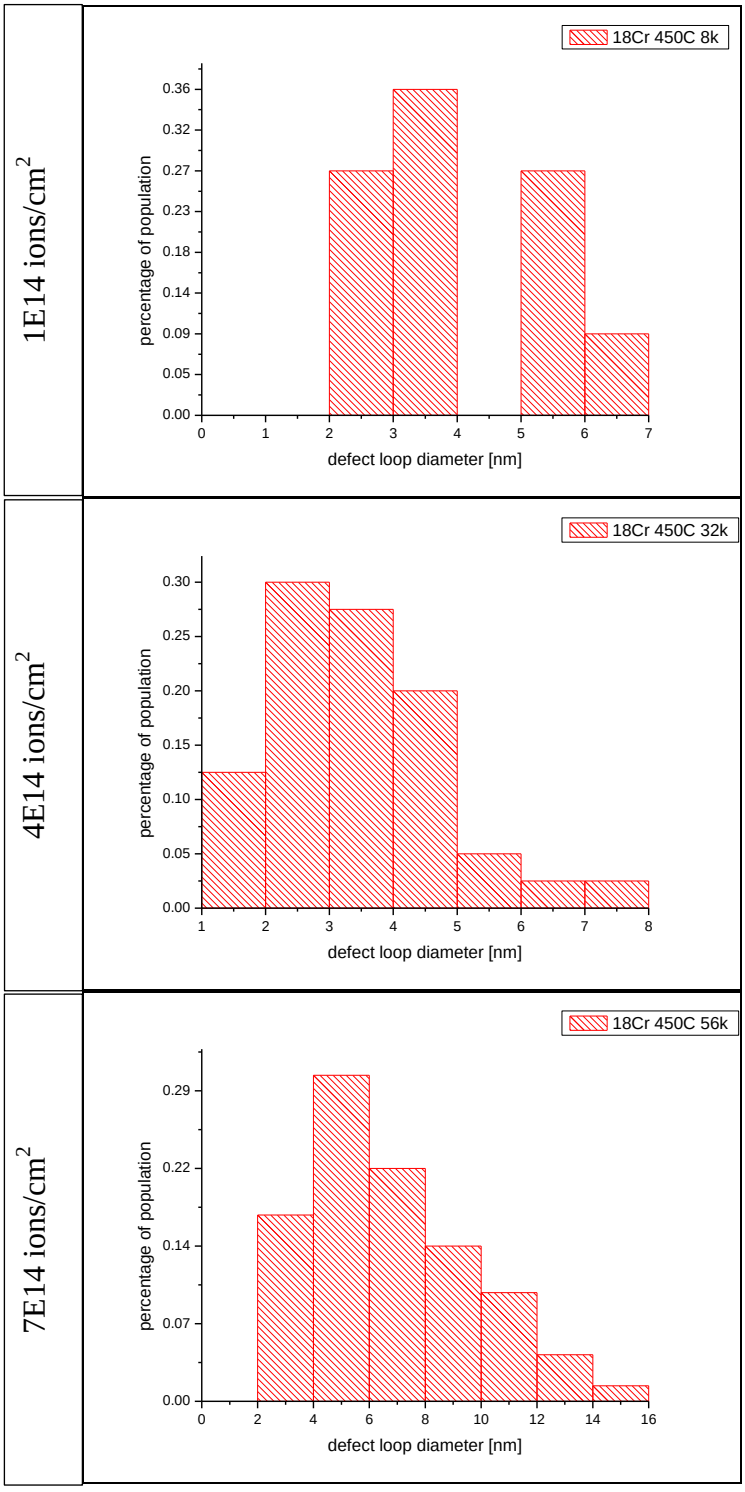

Figure 3.8. Defect population diameters for Fe18Cr irradiated at 450°C at fluence points 1E14-7E14 ions/cm^2, increasing fluence from top to bottom.

As noted previously, these defect size distributions are based on measurements of image size, and are therefore likely to be broadened with respect to the actual defect size distributions. It is also important to note that we believe there to be many defects in the 0-2nm range that are not visible in the TEM, so the true defect size distributions are peaked at the left. It appears that the difference in chromium content between 11% and 18% doesn't much change the way the defected microstructure develops on average, nor does the temperature. We see a broadening of the distributions with increased dose as larger defect loops grow. We can see a sharp difference between these defect size distributions and those shown by Okuniewski for pure iron [6]. The FeCr defect populations are skewed much smaller than those in pure Fe, with a narrower spread.

Chapter 4

ANALYSIS

4.1 EFFECT OF TEMPERATURE

While the work of other researchers has revealed some differences in damage morphologies depending on temperature of irradiations [6,7], we find in this work very little dependency on irradiation temperature. Figure 4.1 shows median defect image sizes and densities with dose for both irradiation temperatures. It appears that defects are more mobile in the 450°C irradiations than in the 300°C ones, leading to the development of larger loop structures with higher dose. The findings for the densities, however, are quite puzzling. We would expect that with the larger loop structures obtained at high dose in the higher temperature irradiation, we would see a correspondingly lower density of defects. We do not find this to be the case.

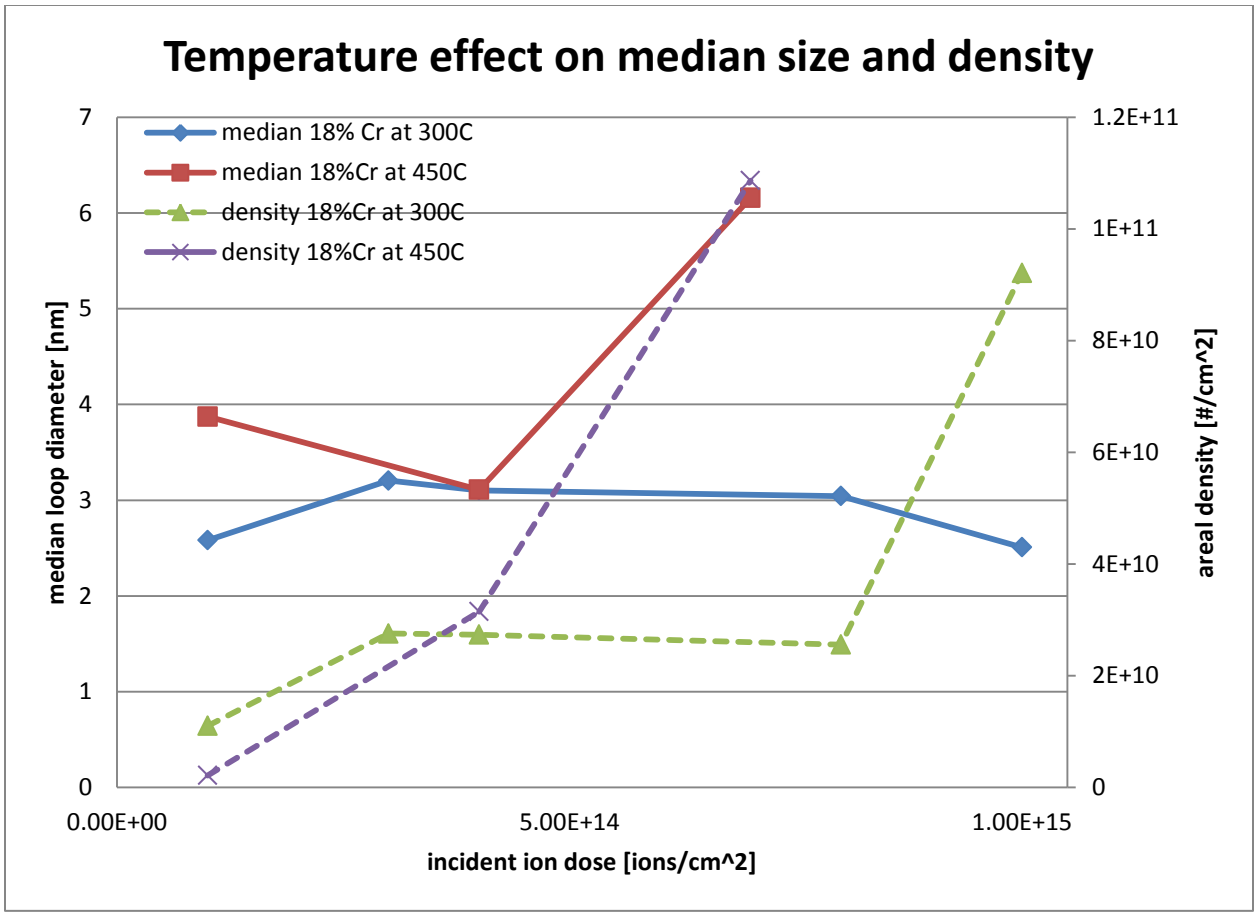

Figure 4.1. Plot of defect mean image sizes (left) and densities (right) for two irradiation temperatures, 300°C and 450°C, as a function of dose.

4.2 EFFECT OF CHROMIUM CONTENT

As discussed in the micrographs section, we find in these experiments a very weak effect of actual chromium content on the evolution of defect loops (though there is a marked difference between 0%Cr and 1X%Cr). When we examine median image size and density information for each of the two chromium concentrations, we see no reliable difference between the two sample compositions.

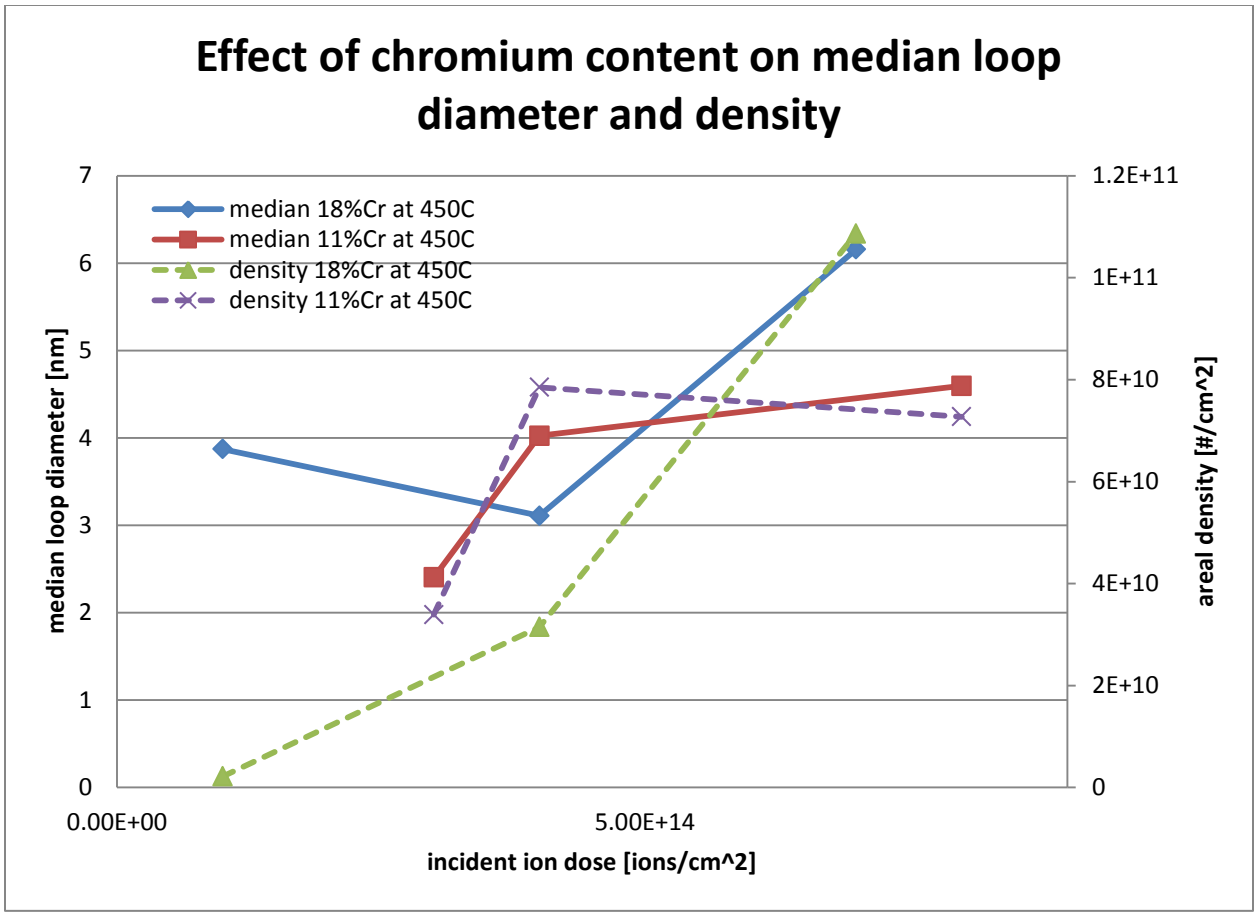

Figure 4.2. Plot of defect mean image sizes (left) and densities (right) for two irradiation chromium contents, Fe11Cr and Fe18Cr, as a function of dose.

Chapter 5

SUMMARY

5.1 Conclusions

In this experiment we examined the microstructural evolution of irradiation induced defects in model FeCr materials and compared it with the evolution of irradiation defected microstructure in pure Fe. Defect loops grow more quickly and develop into complex and nested loop structures in pure Fe, but this development is prevented by the addition of chromium. We found that chromium had the effect of inhibiting defect mobility in the alloy, causing defects to remain small and relatively motionless. The exact mechanism that allows chromium to pin defects is unknown. The behavior of defects in the FeCr alloys, as evidenced by live observations, was to appear as small loops of dot-type contrast, grow a limited amount but not move, and occasionally disappear by gliding to the free surface. We found only a weak dependence of loop morphology on the specific chromium content of the alloy, which is consistent with the results found by Yao [7]. We found there to be little discernable difference between the defect evolution at 300°C and 450°C, with the exception of defect nucleation occurring at lower doses in the lower temperature case. Voids are seen with self-ion irradiation of Fe, but we saw no evidence of void formation in the FeCr alloys. Some of the puzzling results showing defect density dependence on dose can be addressed by acknowledging that there is much error associated with the measurements of sizes of the defects and in identifying what is a defect and what is not. These experiments are most illuminating when looking at qualitative observations surrounding loop mobilities and recombination behavior. This is, after all, the advantage of conducting the work *in situ*. The raw values for defect densities are less useful (and less reliable).

5.2 Future Work

Experiments are underway at the Advanced Test Reactor (ATR-NSUF) at Idaho National Laboratory to perform bulk neutron irradiations on model, commercial, and developmental reactor materials. Among the model materials are pure Fe, Fe14Cr, and Fe19Cr. They will be irradiated with neutrons to doses of 0.01, 0.1, 1, 5, and 10 dpa at temperatures of 300°C, 450°C, and 550°C. Post-irradiation examination will be performed in a TEM in order to characterize the irradiated microstructures.

The neutron-irradiated microstructures will be compared with those produced by the ion irradiations. We will look for validation of the ion irradiation results and examine possible sources of differences in damage morphologies. It is our aim to show that heavy ion irradiations can be used as a surrogate for neutron irradiations in the development of models for Nuclear Engineering, as they can produce the same kind of damage morphologies. We will also be examining the higher temperature effects on the defect microstructure, comparing the results of the irradiations at 550°C with those done at lower temperatures. It is possible that we will see the development of second-phase precipitates at high temperatures. We also plan to perform some mechanical property measurements (such as nanohardness testing) on the neutron irradiated samples in order to relate mechanical properties back to developments in the microstructure.

With an appropriate interatomic Fe-Cr potential, modeling efforts could significantly contribute to the understanding of the damage processes taking place at the microstructural level. Once an appropriate potential is developed, Molecular Dynamics and kinetic Monte Carlo codes will add further insight into how and why the defect microstructure evolves the way it does. Ultimately,

the defect distributions produced by the ion and neutron irradiations can be replicated in kinetic Monte Carlo simulations. These distributions and potentials can then be used for predictive work on irradiation conditions we have not yet examined. These simulations can guide our efforts towards experiments in critical regions of temperature and dose that will allow us to better understand the processes taking place in the microstructure of reactor materials.

BIBLIOGRAPHY

[1] R.L. Klueh and D.R. Harries, *High Chromium Ferritic and Martensitic Steels for Nuclear Applications, American Society for Testing and Materials*, West Conshohocken, PA, 2001.

[2] F.A. Garner, M.B. Toloczko and B.H. Sencer, "Comparison of swelling and irradiation creep behavior of FCC-austenitic and BCC-ferritic/martensitic alloys at high neutron exposure," *Journal of Nuclear Materials*, vol. 276, pp.123-142, 2000.

[3] A. Kohyama, A. Hishinuma, D. S. Gelles, R. L. Klueh, W. Dietz, and K. Ehrlich, "Low-activation ferritic and martensitic steels for fusion application," *Journal of Nuclear Materials*, vol. 233-237A, pp. 138-147, 1996.

[4] D. S. Gelles, "Microstructural examination of commercial ferritic alloys at 200 dpa," *Journal of Nuclear Materials*, vol. 233-237A, pp. 293-298, 1996.

[5] L. K. Mansur, A. F. Rowcliffe, R. K. Nanstad, S. J. Zinkle, W. R. Corwin, R. E. Stoller, "Materials needs for fusion, generation IV fission reactors and spallation neutron sources – similarities and differences," *Journal of Nuclear Materials*, vol. 329-333A, pp. 166-172, 2004.

[6] M. A. Okuniewski, "Irradiation-induced Microstructural Evolution and Mechanical Properties in Iron with and without Helium," Ph.D. dissertation, University of Illinois at Urbana-Champaign, 2004.

[7] Z. Yao, et al, "Heavy ion irradiations of Fe and Fe-Cr model alloys: Part 1: Damage evolution in thin foils at low doses," *Philosophical Magazine*, vol. 88 (21), pp. 2851-2880, 2008.

[8] http://www.msd.anl.gov

[9] G. H. Kinchin and R. S. Pease, "The displacement of atoms in solids by radiation," *Reports on Progress in Physics*, vol. 18, pp. 1-51, 1955.

[10] M. J. Norgett, M. T. Robinson, and I. M. Torrens, "A proposed method of calculating displacement dose rates," *Nuclear Engineering and Design*, vol. 33, pp. 50-54, 1975.

[11] G. S. Was, *Fundamentals of Radiation Mateirals Science*, Springer-Verlag, Berlin, Germany, 2007.

[12] G. S. Was and T. R. Allen, "Radiation damage from different particle types," in *Radiation Effects in Solids: Proceedings of the NATO" Advanced Study Institute on Radiation Effects in Solids.* Erice, Sicily, Italy, July 17-29, 2004. Eds. K. E. Sickafus, E. A. Kotomin, and B. P. Uberuaga. Springer, Dordrecht, The Netherlands, pp. 65-98, 2007.

[13] J. F. Ziegler and J.P. Biersack, SRIM-2003. Vers. 2003.20, 2003.

[14] L. K. Mansur, "Correlation of neutron and heavy-ion damage," *Journal of Nuclear Materials*, vol. 78, pp. 156-160, 1978.

[15] L. K. Mansur, "Void swelling in metals and alloys under irradiation: An assessment of the theory," *Nuclear Technology*, vol. 40, pp. 5-34, 1978.

[16] L. K. Mansur, "Theory and experimental background on dimensional changes in irradiated alloys," *Journal of Nuclear Materials*, vol. 216, pp. 97-123, 1994.

[17] P. B. Hirsch, A. Howie, R. B. Nicholson, D. W. Pashley, and M. J. Whelan, *Electron Microscopy of Thin Crystals*, Plenum Press, New York, 1965.

[18] D. B. Williams and C. B. Carter, *Transmission Eelctron Microscopy: A Textbook for Materials Science*, Springer Science + Business Media, Inc., New York, New York, 1996.

[19] J. W. Edington, *Practical Electron Microscopy in Materials Science*, Van Nostrand Reinhold Company, New York, New York, 1976.

[20] M. L. Jenkins and M. A. Kirk, *Characterization of Radiation Damage by Transmission Electron Microscopy*, Institute of Physics Publishing, Bristol, England, 2001.

[21] M.L. Jenkins, M.A. Kirk, and H. Fukushima, "On the application of the weak-beam technique to the determination of the sizes of small point-defect clusters in ion-irradiated copper," *Journal of Electron Microscopy*, vol. 48, pp. 323-332, 1999.

[22] M.A. Kirk, M.L. Jenkins, and H. Fukushima, "The search for interstitial dislocation loops produced in displacement cascades at 20 K in copper," *Journal of Nuclear Materials*, vol. 276, pp. 50-58, 2000.

[23] Z. Zhou, M. L. Jenkins, S. L. Dudarev, A. P. Sutton, and M. A. Kirk, "Simulations of weak-beam diffraction contrast images of dislocation loops by the many-beam Howie–Basinski equation," *Philosophical Magazine*, vol 86, pp. 4851-4881, 2006.

[24] Z. Yao, M. L. Jenkins, and M. A. Kirk, Personal communication, 2008.

[25] W. S. Rasband, ImageJ, U. S. National Institutes of Health, Bethesda, Maryland, USA, http://imagej.nih.gov/ij/, 1997-2011.

Author's Biography

Carolyn Anne Tomchik received her Bachelors of Science in Nuclear Engineering in May of 2005. She received the Harvey H. Jordan award for an outstanding senior in the College of Engineering and was awarded Bronze Tablet honors. Carolyn also received the award of Knight of St. Patrick for exemplary contributions and service to the College of Engineering. She completed her Masters of Science degree under the guidance of her advisor, Professor James F. Stubbins. As a graduate student, Carolyn has been the recipient of the Carver Fellowship, the Department of Energy's Nuclear Engineering and Health Physics Fellowship, and the University of Illinois Nuclear Engineering Fellowship funded by the Nuclear Regulatory Commission. She is pursuing her Ph.D. in Nuclear Engineering under Prof. James F. Stubbins in the area of irradiation damage in nuclear structural materials.